Supplementary information

Delicate ternary heterostructures achieved by hierarchical co-assembly of Ag and Fe_3O_4 nanoparticles on MoS_2 nanosheets: morphological and compositional synergies on reversible lithium storage

Long Pan,[a] Xiao-Dong Zhu,[b] Xu-Ming Xie [a] and Yi-Tao Liu [a]

[a]Key Laboratory of Advanced Materials (MOE), Department of Chemical Engineering, Tsinghua University, Beijing 100084, China

[b]Academy of Fundamental and Interdisciplinary Sciences, Harbin Institute of Technology, Harbin 150080, China

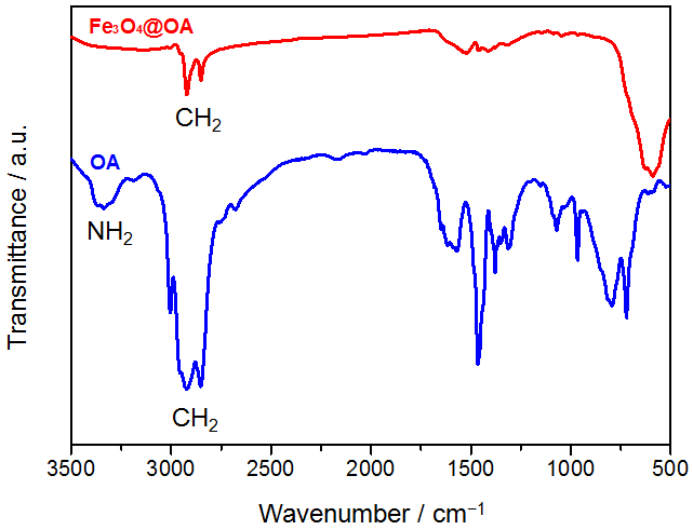

Figure S1 − FTIR spectra of oleylamine (OA) and Fe_3O_4@OA NPs. The successful complexation between Fe_3O_4 and the NH_2 group of OA is confirmed, since the peak characteristic of NH_2 stretching disappears, while the CH_2 stretching peak remains in the FTIR spectrum of Fe_3O_4@OA NPs.

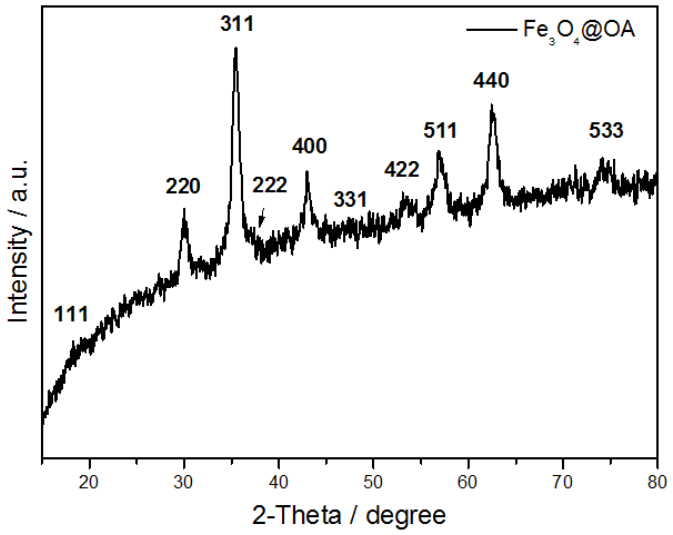

Figure S2 − XRD pattern of Fe_3O_4@OA NPs showing well-resolved peaks (111, 220, 311, 222, 400, 331, 422, 511, 440 and 533) of spinel Fe_3O_4 (JCPDS card No. 19−0629).

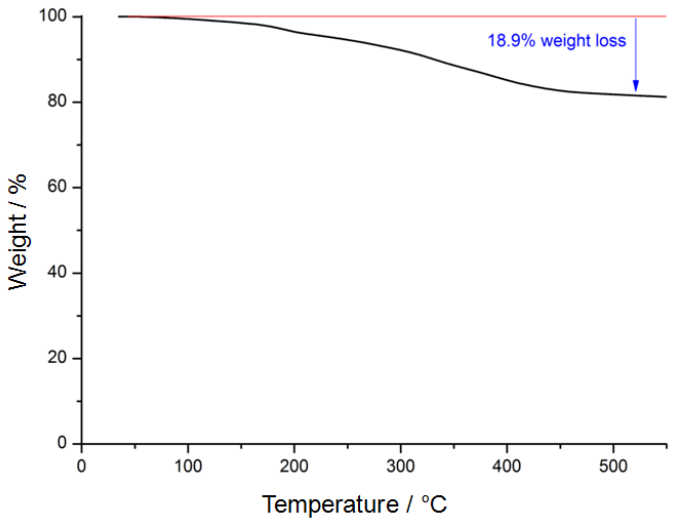

Figure S3 − TGA curve of Fe_3O_4@OA NPs showing 18.9 wt% OA content.

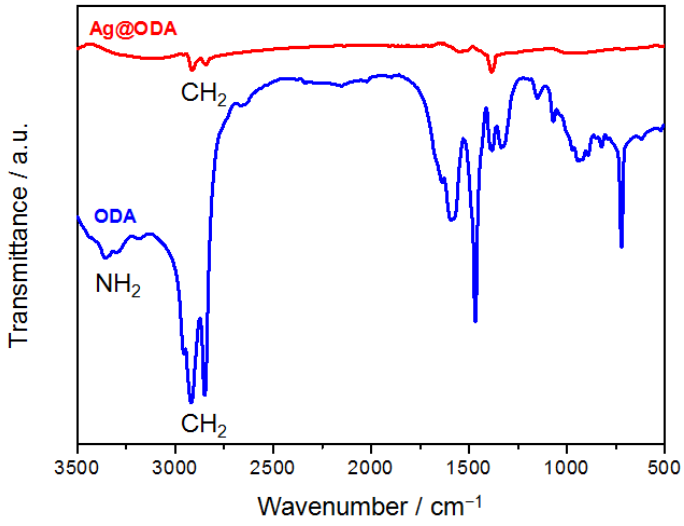

Figure S4 − FTIR spectra of octadecylamine (ODA) and Ag@ODA NPs. The successful complexation between Ag and the NH_2 group of ODA is confirmed, since the peak characteristic of NH_2 stretching disappears, while the CH_2 stretching peak remains in the FTIR spectrum of Ag@ODA NPs.

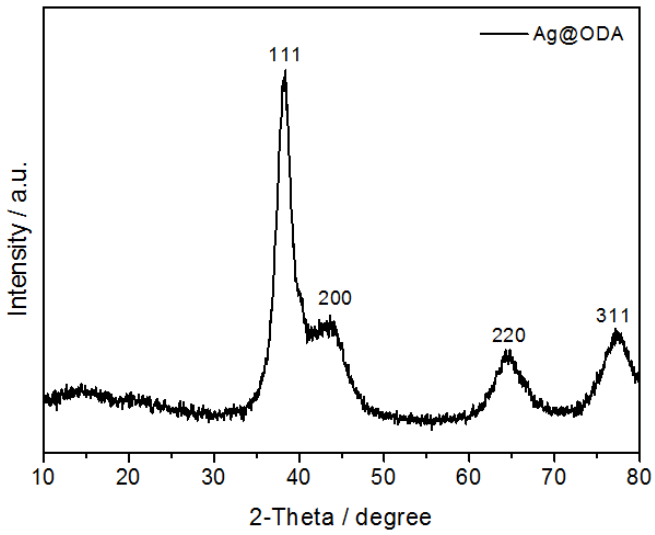

Figure S5 − XRD pattern of Ag@ODA NPs showing well-resolved peaks (111, 200, 220 and 311) of face-centered cubic (fcc) Ag (JCPDS card No. 87−0720).

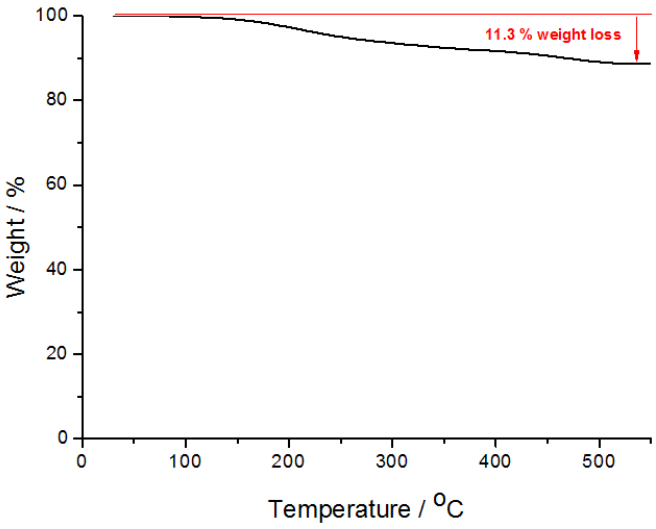

Figure S6 − TGA curve of Ag@ODA NPs showing 11.3 wt% ODA content.

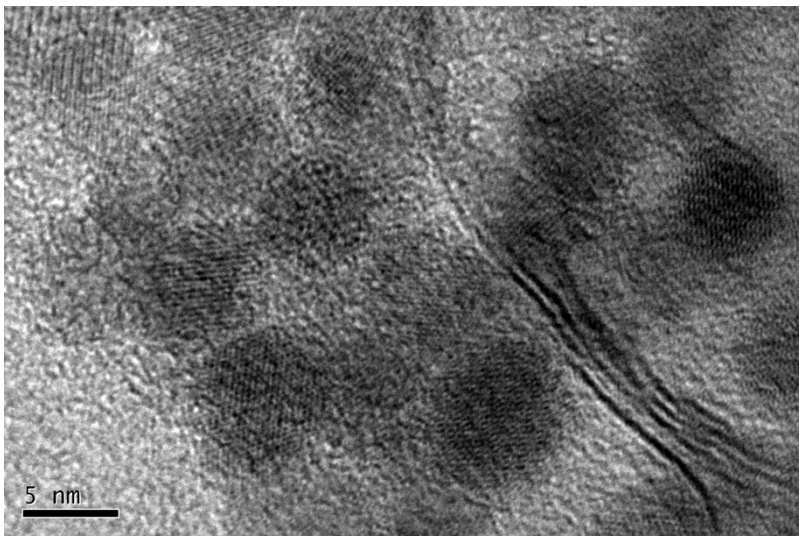

Figure S7 − HRTEM image of Fe_3O_4−MoS_2 binary heterostructures.

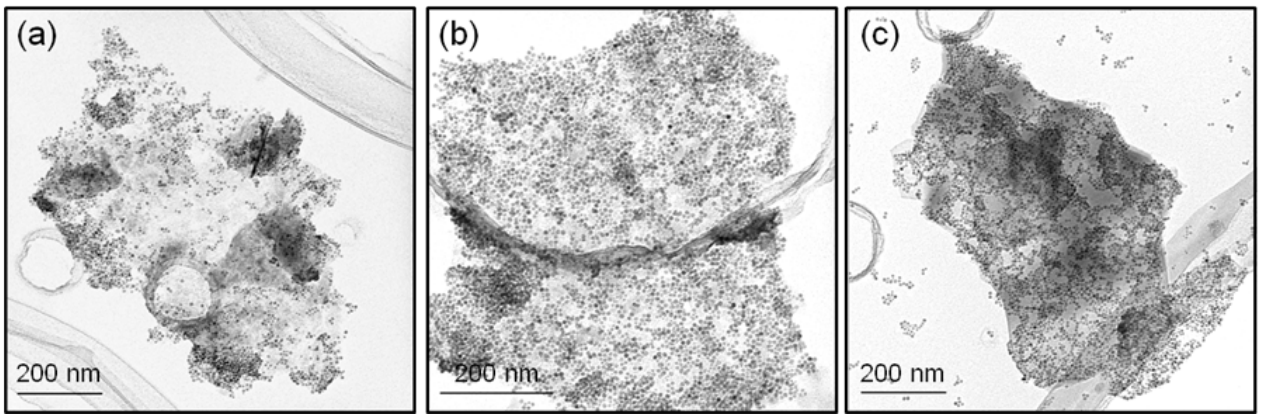

Figure S8 − TEM images of Fe_3O_4−MoS_2 binary heterostructures at a wt ratio of (a) 2:10, (b) 5:10 and (c) 8:10.

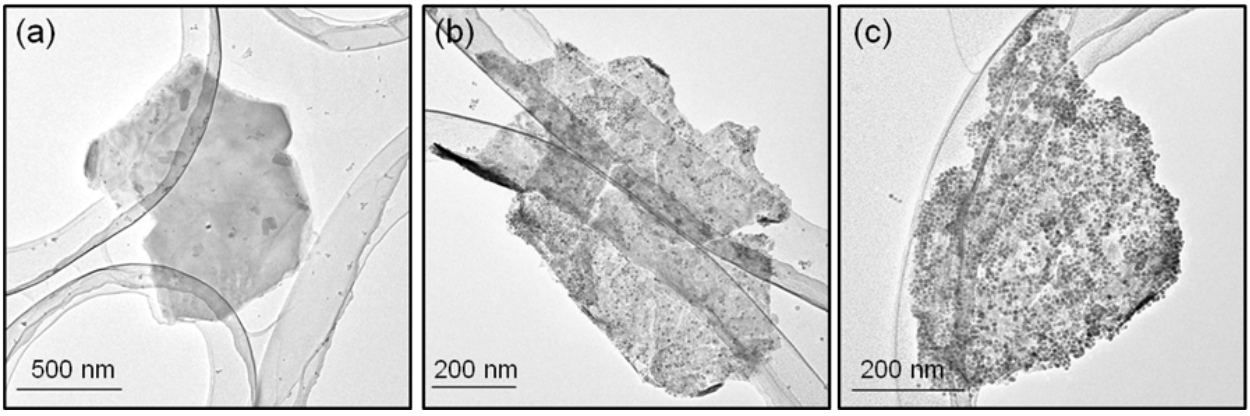

Figure S9 − TEM images showing the results of an interesting control experiment, in which the Fe_3O_4@OA NPs are tried to be assembled on the MoS_2 nanosheets (5:10) in a mixture of NMP and THF at a vol ratio of (a) 95:5, (b) 90:10 and (c) 50:50. It is apparent that the higher the THF fraction, the more successful the NP adhesion. When the THF fraction is only 5%, the NP adhesion is prohibited due to the adequate solvation of MoS_2 nanosheets that minimizes the surface energy. At a slightly elevated THF fraction, the NPs sparsely adhere to the MoS_2 surfaces. When the THF fraction is high enough (50%), uniform and dense decoration of the MoS_2 nanosheets with the NPs can be achieved.

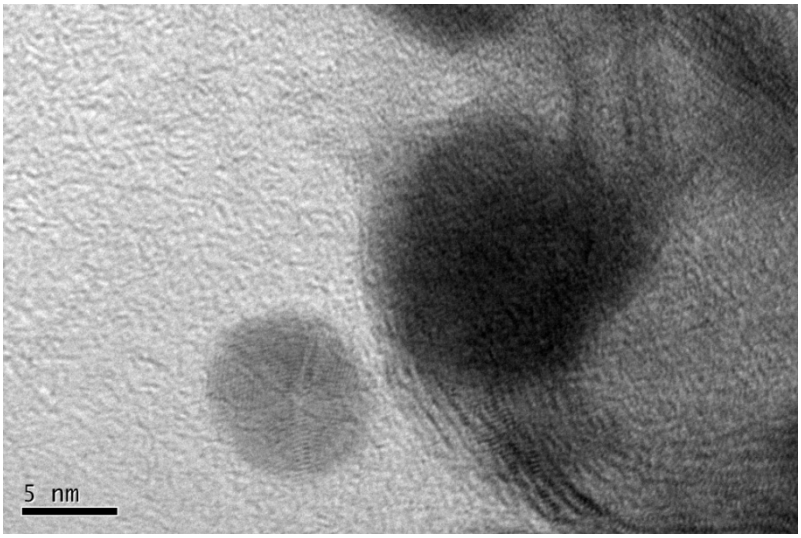

Figure S10 − HRTEM image of Ag−MoS_2 binary heterostructures.

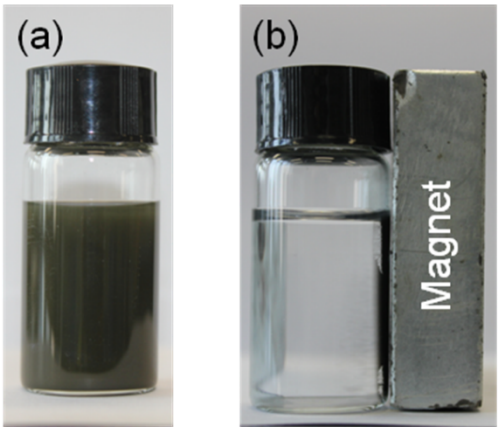

Figure S11 − Photographs of a THF solution of Ag/Fe_3O_4−MoS_2 ternary heterostructures (a) before and (b) after magnetic attraction.

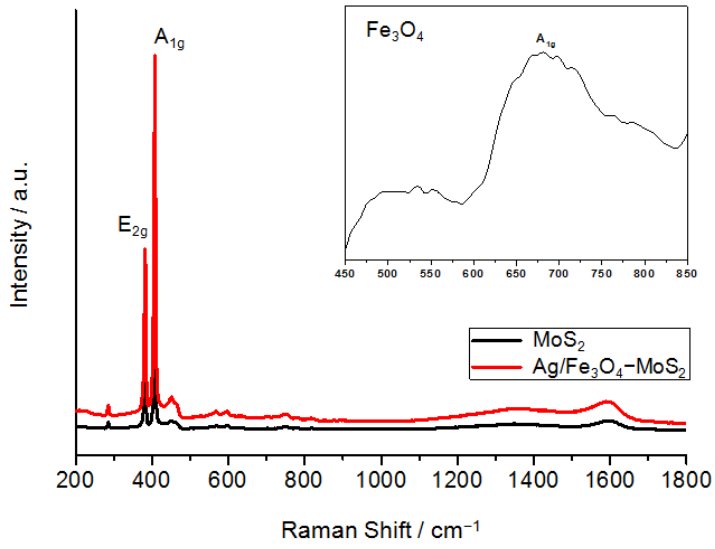

Figure S12 − Raman spectra of neat MoS_2 nanosheets and Ag/Fe_3O_4−MoS_2 ternary heterostructures. Insert: Raman spectrum of Fe_3O_4@OA NPs. Seen from the figure, the two characteristic peaks of MoS_2 at 381 and 408 cm^{-1}, corresponding to the in-plane E_{2g} and out-of-plane A_{1g} vibrations, can be easily recognized. It is found, interestingly, that the Raman intensity of Ag/Fe_3O_4−MoS_2 ternary heterostructures increases significantly compared to that of neat MoS_2 nanosheets, confirming the surface-enhanced Raman scattering (SERS) effect of Ag present in the ternary heterostructures. Note that the Raman signals of Fe_3O_4@OA NPs are absent in the Ag/Fe_3O_4−MoS_2 ternary heterostructures due to the much weaker Raman intensity of Fe_3O_4 than MoS_2.

Table S1 − Elemental composition of Ag/Fe_3O_4−MoS_2 ternary heterostructures.

	Fe (wt%)	Ag (wt%)	Ag@ODA (wt%)	Fe_3O_4@OA (wt%)	MoS_2 (wt%)
Actual ratio	17.52	5.86	6.61	29.89	63.50[a)]
Starting ratio	−	−	6.25	31.25	62.50

[a)]Note that MoS_2 cannot be completely dissolved in concentrated H_2SO_4 at ambient temperature, so its accurate composition is calculated by subtracting those of Ag@ODA and Fe_3O_4@OA NPs from 100 wt%.

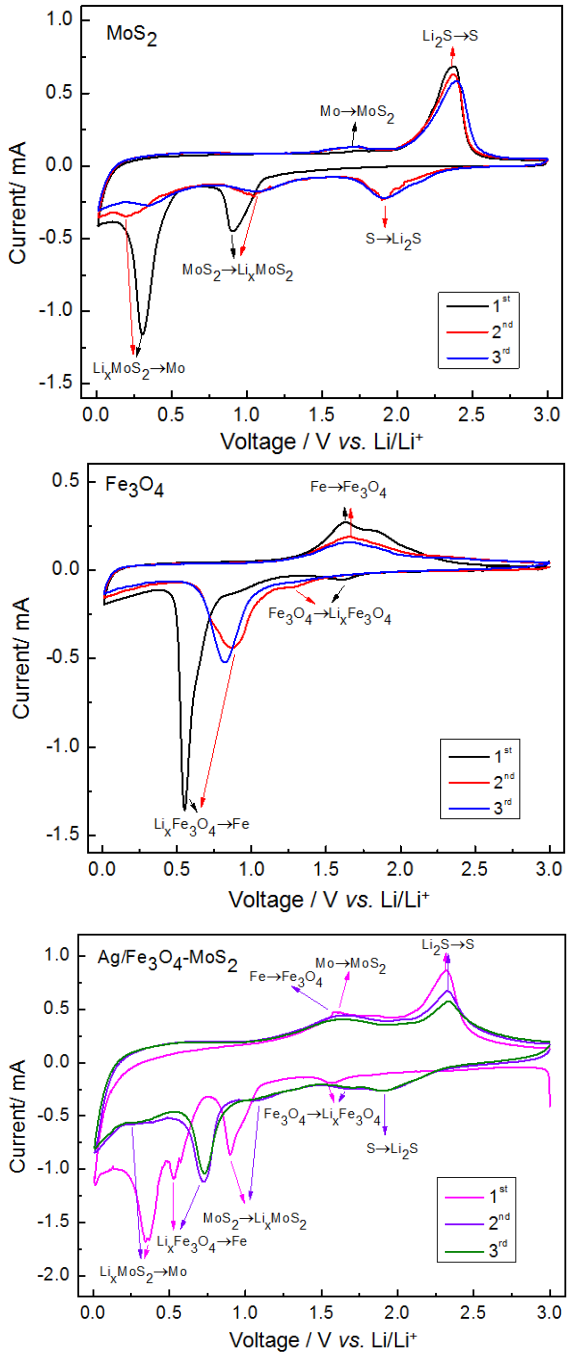

Figure S13 – A comparison among the first three CV curves of neat MoS_2, Fe_3O_4 and Ag/Fe_3O_4–MoS_2 ternary heterostructures. As seen from the CV curves of Ag/Fe_3O_4–MoS_2 ternary heterostructures, the reduction peaks at 1.57 and 0.90 V in the first cathodic scan originate from the formation of $Li_xFe_3O_4$ and Li_xMoS_2 due to Li^+ ion intercalation. The reduction peak at 0.53 V corresponds to the conversion reaction of Fe^{3+} and Fe^{2+} to Fe^0. The strong reduction peak at 0.34 V is related to the kinetically activated electrolyte degradation and the conversion reaction, in which Mo^{4+} is reduced to Mo^0. In the subsequent sweeps, the

obvious peak at 0.34 V becomes inconspicuous, indicating that the SEI layer has been built perfectly. The other three reduction peaks are positively shifted in the second and third cathodic sweeps due to the structural modification after the first cycle.[1] The reduction peaks at 0.72, 1.10 and 1.64 V are attributed to the following three reactions: $Li_xFe_3O_4 + (8-x)Li^+ + (8-x)e^- \rightarrow 3Fe + 4Li_2O$, $MoS_2 + xLi^+ + xe^- \rightarrow Li_xMoS_2$, and $Fe_3O_4 + xLi^+ + xe^- \rightarrow Li_xFe_3O_4$, respectively. During the second cathodic scan, a new reduction peak at ~1.90 V arises, which is related to the reaction of $Mo + 4Li^+ + 2S + 4e^- \rightarrow 2Li_2S + Mo$. In the anodic scan, the reverse oxidation peak at 2.32 V corresponds to the conversion of S^{2-} to S^0.[2] However, the broad oxidation peak at 1.54−1.86 V is the overlapping of two oxidation peaks, which stand for the partial oxidation of Mo to MoS_2 and the oxidation of Fe to Fe_3O_4. From the second anodic and cathodic scans, both the peak current and the integrated area intensity are nearly unchanged, indicating there is a very tiny capacity loss during charging. The CV measurements therefore confirm the good electrochemical activity and stability of the Ag/Fe_3O_4−MoS_2 anode.

[1] T. Yoon, C. Chae, Y.-K. Sun, X. Zhao, H. H. Kung and J. K. Lee, *J. Mater. Chem.*, 2011, **21**, 17325.

[2] L. Pan, Y.-T. Liu, X.-M. Xie and X.-D. Zhu, *Chem. Asian J.*, 2014, **9**, 1519.

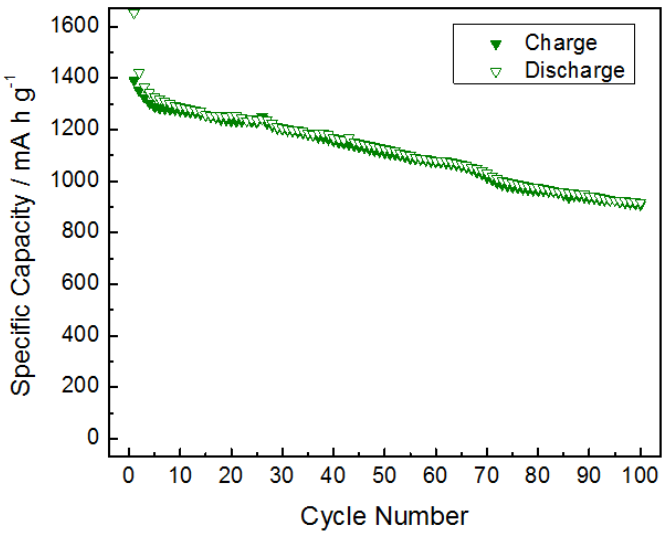

Figure S14 − Cycle behavior of Fe_3O_4−MoS_2 binary heterostructures at a current density of 200 mA g^{-1}.

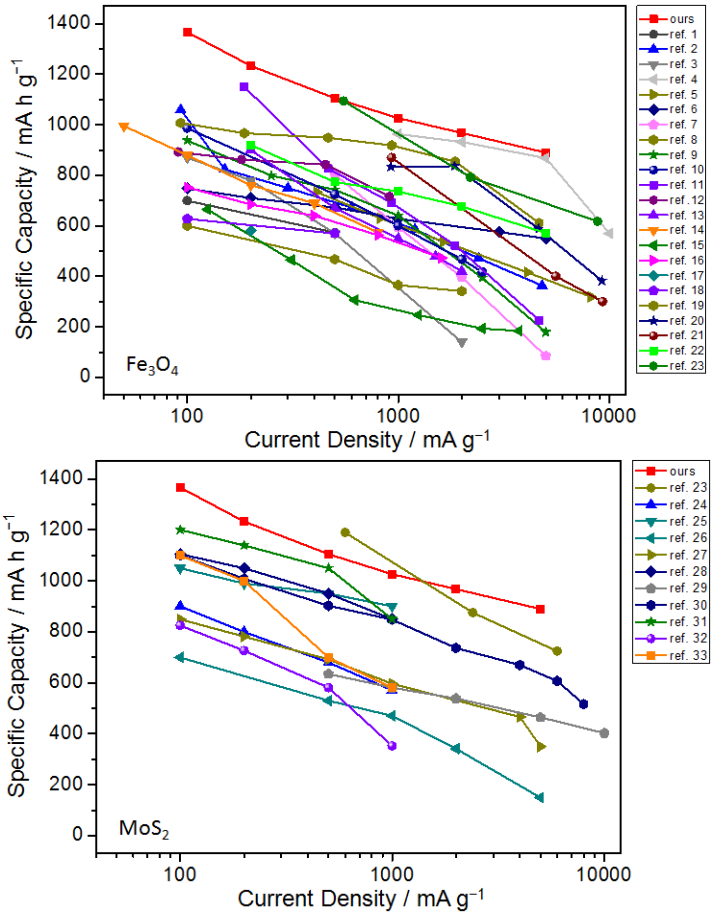

Figure S15 − A comparison among the rate capabilities of our Ag/Fe_3O_4−MoS_2 anode and various Fe_3O_4 or MoS_2 anodes previously reported.

[1] Y. Chen, H. Xia, L. Lu and J. Xue, *J. Mater. Chem.*, 2012, **22**, 5006.

[2] W. Wei, S. Yang, H. Zhou, I. Lieberwirth, X. Feng and K. Müllen, *Adv. Mater.*, 2013, **25**, 2909.

[3] T. Yoon, C. Chae, Y.-K. Sun, X. Zhao, H. H. Kung and J. K. Lee, *J. Mater. Chem.*, 2011, **21**, 17325.

[4] C. He, S. Wu, N. Zhao, C. Shi, E. Liu and J. Li, *ACS Nano*, 2013, **7**, 4459.

[5] S. Saadat, J. Zhu, D. H. Sim, H. H. Hng, R. Yazami and Q. Yan, *J. Mater. Chem. A*, 2013, **1**, 8672.

[6] B. Jang, M. Park, O. B. Chae, S. Park, Y. Kim, S. M. Oh, Y. Piao and T. Hyeon, *J. Am. Chem. Soc.*, 2012, **134**, 15010.

[7] C. Lei, F. Han, D. Li, W.-C. Li, Q. Sun, X.-Q. Zhang and A.-H. Lu, *Nanoscale*, 2013, **5**, 1168.

[8] T. Yoon, J. Kim, J. Kim and J. K. Lee, *Energies*, 2013, **6**, 4830.

[9] J. Ming, J.-B. Park and Y.-K. Sun, *ACS Appl. Mater. Interfaces*, 2013, **5**, 2133.

[10] J. E. Lee, S.-H. Yu, D. J. Lee, D.-C. Lee, S. I. Han, Y.-E. Sung and T. Hyeon, *Energy Environ. Sci.*, 2012, **5**, 9528.

[11] S. Jin, H. Deng, D. Long, X. Liu, L. Zhan, X. Liang, W. Qiao and L. Ling, *J. Power Sources*, 2011, **196**, 3887.

[12] Z. Xiao, Y. Xia, Z. Ren, Z. Liu, G. Xu, C. Chao, X. Li, G. Shen and G. Han, *J. Mater. Chem.*, 2012, **22**, 20566.

[13] R. Wang, C. Xu, J. Sun, L. Gao and C. Lin, *J. Mater. Chem. A*, 2013, **1**, 1794.

[14] D. Chen, G. Ji, Y. Ma, J. Y. Lee and J. Lu, *ACS Appl. Mater. Interfaces*, 2011, **3**, 3078.

[15] L. Lang and Z. Xu, *ACS Appl. Mater. Interfaces*, 2013, **5**, 1698.

[16] S. H. Lee, S.-H. Yu, J. E. Lee, A. Jin, D. J. Lee, N. Lee, H. Jo, K. Shin, T.-Y. Ahn, Y.-W. Kim, H. Choe, Y.-E. Sung and T. Hyeon, *Nano Lett.*, 2013, **13**, 4249.

[17] B. Wang, H. B. Wu, L. Zhang and X. W. Lou, *Angew. Chem. Int. Ed.*, 2013, **52**, 4165.

[18] Y. Chen, B. H. Song, L. Lu and J. M. Xue, *Mater. Technol.*, 2013, **28**, 254.

[19] Q. Q. Xiong, J. P. Tu, Y. Lu, J. Chen, Y. X. Yu, Y. Q. Qiao, X. L. Wang and C. D. Gu, *J. Phys. Chem. C*, 2012, **116**, 6495.

[20] S. Wu, Z. Wang, C. He, N. Zhao, C. Shi, E. Liu and J. Li, *J. Mater. Chem. A*, 2013, **1**, 11011.

[21] J. Luo, J. Liu, Z. Zeng, C. F. Ng, L. Ma, H. Zhang, J. Lin,Z. Shen and H. J. Fan, *Nano Lett.*, 2013, **13**, 6136.

[22] Y. Su, S. Li, D. Wu, F. Zhang, H. Liang, P. Gao, C. Cheng and X. Feng, *ACS Nano*, 2012, **6**, 8349.

[23] Y. Gong, S. Yang, Z. Liu, L. Ma, R. Vajtai and P. M. Ajayan, *Adv. Mater.*, 2013, **25**, 3979.

[24] Z. Wang, T. Chen, W. Chen, K. Chang, L. Ma, G. Huang, D. Chen and J. Y. Lee, *J. Mater. Chem. A*, 2013, **1**, 2202.

[25] K. Chang and W. Chen, *ACS Nano*, 2011, **5**, 4720.

[26] V. H. Phama, K. H. Kim, D. W. Jung, K. Singh, E. S. Oh and J. S. Chung, *J. Power Sources*, 2013, **244**, 280.

[27] X. Cao, Y. Shi, W. Shi, X. Rui, Q. Yan, J. Kong and H. Zhang, *Small*, 2013, **9**, 3433.

[28] K. Chang and W. Chen, *J. Mater. Chem.*, 2011, **21**, 17175.

[29] X. Zhou, L.-J. Wan and Y.-G. Guo, *Chem. Commun.*, 2013, **49**, 1838.

[30] H. Yu, C. Ma, B. Ge, Y. Chen, Z. Xu, C. Zhu, C. Li, Q. Ouyang, P. Gao, J. Li, C. Sun, L. Qi, Y. Wang and F. Li, *Chem. Eur. J.*, 2013, **19**, 5818.

[31] K. Chang, D. Geng, X. Li, J. Yang, Y. Tang, M. Cai, R. Li and X. Sun, *Adv. Energy Mater.*, 2013, **3**, 839.

[32] S. Ding, D. Zhang, J. S. Chen and X. W. Lou, *Nanoscale*, 2012, **4**, 95.

[33] C. Zhang, Z. Wang, Z. Guo and X. W. Lou, *ACS Appl. Mater. Interfaces*, 2012, **4**, 3765.